Astronomical tunings of the Oligocene-Miocene Transition from Pacific Ocean Site U1334 and implications for the carbon cycle

Helen M. Beddow[1], Diederik Liebrand[2, 3, *], Douglas S. Wilson[4], Frits J. Hilgen[1], Appy Sluijs[1], Bridget S. Wade[5], Lucas J. Lourens[1]

[1]*Department of Earth Sciences, Faculty of Geosciences, Utrecht University, Utrecht, The Netherlands;* [2]*PalaeoClimate.Science, Utrecht (province), The Netherlands* [3]*MARUM - Center for Marine Environmental Science, University of Bremen, Bremen, Germany;* [4]*Department of Earth Science University of California, Santa Barbara (CA), United States;* [5]*Department of Earth Sciences, Faculty of Mathematical and Physical Sciences, University College London, Gower Street, London, United Kingdom;* [*]Corresponding author: diederik@palaeoclimate.science

Abstract

Astronomical tuning of sediment sequences requires both unambiguous cycle-pattern recognition in climate proxy records and astronomical solutions, and independent information about the phase relationship between these two. Here we present two different astronomically tuned age models for the Oligocene-Miocene Transition (OMT) from Integrated Ocean Drilling Program Site U1334 (equatorial Pacific Ocean) to assess the effect tuning has on astronomically calibrated ages and the geologic time scale. These alternative age models (roughly from ~22 to ~24 Ma) are based on different tunings between proxy

records and eccentricity: the first age model is based on an aligning $CaCO_3$ weight (wt%) to Earth's orbital eccentricity, the second age model is based on a direct age calibration of benthic foraminiferal stable carbon isotope ratios ($\delta^{13}C$) to eccentricity. To independently test which tuned age model and associated tuning assumptions is in best agreement with independent ages based on tectonic plate-pair spreading rates, we assign the tuned ages to magnetostratigraphic reversals identified in deep-marine magnetic anomaly profiles. Subsequently, we compute tectonic plate-pair spreading rates based on the tuned ages. The resultant, alternative spreading rate histories indicate that the $CaCO_3$ tuned age model is most consistent with a conservative assumption of constant, or linearly changing, spreading rates. The $CaCO_3$ tuned age model thus provides robust ages and durations for polarity chrons C6Bn.1n–C7n.1r, which are not based on astronomical tuning in the latest iteration of the Geologic Time Scale. Furthermore, it provides independent evidence that the relatively large (several 10,000 years) time lags documented in the benthic foraminiferal isotope records relative to orbital eccentricity, constitute a real feature of the Oligocene-Miocene climate system and carbon cycle. The age constraints from Site U1334 thus provide independent evidence that the delayed responses of the Oligocene-Miocene climate-cryosphere system and (marine) carbon cycle resulted from highly nonlinear feedbacks to astronomical forcing.

Keywords

Astronomical tuning, marine carbon cycle, Oligocene Miocene Transition, IODP Site U1334, equatorial Pacific Ocean, geologic time scale

1. Introduction

Astronomically tuned age models are important in studies of Cenozoic climate change, because they shed light on cause and effect relationships between insolation forcing and the linear and nonlinear responses of Earth's climate system (e.g., [*Hilgen et al.*, 2012, *Vandenberghe et al.*, 2012; *Westerhold et al.,* 2017]). As more Cenozoic paleoclimate records are generated that use astronomical tuning as the main high-precision dating tool, it is important to understand the assumptions and limitations inherent in this age-calibration method, in particular with respect to assumptions related to phase-relationships between tuning signal and target curves (i.e., climate proxy records and astronomical solutions, respectively). These phase assumptions have implications for (*i*) determining the absolute timing of events, (*ii*) the understanding of leads and lags in the climate system, and (*iii*) the exact astronomical frequencies that are present in climate proxy records after tuning.

Previously published astronomically tuned age-models for high-resolution climate records that span the Oligocene-Miocene Transition (OMT, ~23 Ma), have used different tuning signal curves for sites from different paleoceanographic settings. In addition, different tuning target curves have been applied. For example, records from Ocean Drilling Program (ODP) Sites 926 and 929 from the Ceara Rise (equatorial Atlantic) were tuned using magnetic susceptibility and/or color reflectance records (i.e., proxies for bulk sediment carbonate content) as tuning signal curve, and used obliquity as the main tuning target curve, sometimes with weaker precession and eccentricity components added (e.g. [*Pälike et al.*, 2006a; *Shackleton et al.*, 1999, 2000; *Zachos et al.*, 2001]). In contrast, sediments from ODP Site 1090 from the Agulhas Ridge (Atlantic sector of the Southern Ocean) and ODP Site 1218 from the equatorial Pacific Ocean were tuned using benthic foraminiferal stable oxygen ($\delta^{18}O$) and/or carbon ($\delta^{13}C$) isotope records as tuning signal (e.g. [*Billups et al.*, 2004; *Pälike et al.*, 2006b]). These records used different combinations of eccentricity, obliquity and/or precession as tuning targets (ETP curves).

More recently, Oligocene-Miocene records from ODP Site 1264 and Middle Miocene records from Integrated Ocean Drilling Program (IODP) Site U1335 used the Earth's eccentricity solution as the sole tuning target. These studies used lithological data, such as elemental estimates based on X-ray fluorescence (XRF) core scanning records, as the sole tuning signal. The records from both these sites are characterized by a clear expression of eccentricity, either resulting from productivity dominated cycles (at Site 1264, [*Liebrand et al*., 2016]) or dissolution dominated cycles (at Site U1335, [*Kochhann et al*., 2016]). The general phase relationships between the ~110-ky cycles and 405-ky cycles (in case of Site U1335), in lithologic records and the stable eccentricity solution for this interval [*Laskar et al*., 2010, *Laskar et al*., 2011], i.e., whether maxima in signal-curve correspond to minima or maxima in target-curve, were straightforward to derive [*Liebrand et al*, 2016, *Kochhann et al*., 2016]. These broad scale phase relationships were in agreement with those previously derived using benthic foraminiferal $\delta^{18}O$ and $\delta^{13}C$ records (e.g., [*Zachos et al*, 2001, *Pälike et al*, 2006b]).

The different options for astronomical age calibration of the Oligocene-Miocene time interval has resulted in large variations in the precise phase-estimates after tuning between ~110-ky and 405-ky cycles present in both the eccentricity solution and in lithologic and climatologic proxy records. In addition, the choice of tuning signal curve may result in different cyclostratigraphic interpretations, and different ages and durations of geologic events. To obtain better constraints for the true phase-relationships of the ~110-ky and 405-ky cycles between benthic foraminiferal stable isotope records and orbital eccentricity, and to better understand the implications that initial phase-assumptions for astronomical age calibration have on absolute ages across the OMT, we need independent dates that are free from tuning phase-assumptions. Previous studies have successfully used plate-pair spreading rates to date magnetochron reversals and used these ages as independent age control (e.g., [*Hilgen et al*., 1991, *Lourens et al*., 2004]).

Here, we present two astronomically tuned age models for newly presented (estimates of) sediment $CaCO_3$ content and previously published high-resolution benthic foraminiferal $\delta^{18}O$ and $\delta^{13}C$ records across the OMT from IODP Site U1334 (eastern equatorial Pacific Ocean) [*Beddow et al.,* 2016]. We select the sediment $CaCO_3$ content and benthic foraminiferal $\delta^{13}C$ as tuning signals, because these data are generally thought represent two end-members in terms of tuning phase assumptions [*Pälike et al*., 2006, *Liebrand et al*., 2016]. We evaluate the ramifications of using these different tuning proxies for (*i*) absolute ages of magnetochron reversals, and (*ii*) the leads and lags between eccentricity tuning target and lithologic/paleoclimate tuning signals. We achieve this, by computing the spreading rate histories of a suite of tectonic plate-pairs, after assigning the astronomically tuned ages to the magnetostratigraphic reversals in their anomaly profiles. The constraints given by the long-term evolutions of these alternative spreading-rate histories are sufficiently precise to discriminate between tuning options and phase assumptions.

2. Materials and Methods

2.1 Site description

Site U1334, located in the eastern equatorial Pacific (4794 meters below sea level (mbsl), 7°59.998′N, 131°58.408′W), was recovered during IODP Expedition 320 (Fig. 1). Upper Oligocene and lower Miocene sediments from Site U1334 were deposited at a paleodepth of ~4200 mbsl and consist of foraminifer- and radiolaria-bearing nannofossil ooze and chalk [*Pälike et al*., 2010, 2012]. An expanded Oligocene-Miocene section with a well-defined magnetostratigraphy was recovered [*Pälike et al*., 2010; *Channell et al*., 2013], and a continuous spliced record of Holes A, B and C was placed on a core composite depth scale below seafloor (CCSF-A, equivalent to meters composite depth; Figs. 2 and 3) [*Westerhold et al*., 2012a]. Samples were taken along the splice and all results presented here follow this depth model [*Beddow et al*., 2016].

2.2 Coulometric $CaCO_3$ and magnetic susceptibility

Lithological records from Site U1334 that span the OMT show large variability in $CaCO_3$ content [*Pälike et al.*, 2010]. To obtain a high-resolution and continuous lithological proxy record, we estimate $CaCO_3$ wt% of the dry sediment (hereafter: $CaCO_3$ content), by calibrating high-resolution shipboard magnetic susceptibility data (MS) to lower resolution discrete shipboard coulometric $CaCO_3$ measurements for Site U1334 [*Pälike et al.*, 2010]. Minimum MS values correspond to maximum $CaCO_3$ values. The correlation between coulometric $CaCO_3$ measurements and MS was calculated using a linear regression line, with an R^2 value of 0.92 (Fig. 2), indicating that ~90% of the variability in the MS record is caused by changes in the bulk sediment $CaCO_3$ content. Middle Miocene $CaCO_3$ records from nearby Site

U1335 show negatively skewed cycle shapes and have been interpreted as a dissolution-dominated signal [*Herbert*, 1994, *Kochhann et al*., 2016]. In contrast, cycle shapes in the $CaCO_3$ content record for the Oligocene-Miocene of Site U1334 are less skewed, suggesting that here $CaCO_3$ content was predominantly controlled by a combination of productivity and dissolution.

2.3 Benthic foraminiferal stable isotope records and magnetostratigraphic age model

We use the benthic foraminiferal $\delta^{18}O$ and $\delta^{13}C$ records of Site U1334, which were measured on the *Oridorsalis umbonatus* and *Cibicidoides mundulus* benthic foraminifer species [*Beddow et al*., 2016]. To construct this mixed-species record, *O. umbonatus* values were corrected to *C. mundulus* values based on ordinary least squares linear regression that was based on the analysis of 180 pairs of for inter-species isotope value comparison was applied (for details see [*Beddow et al*., 2016]). The benthic foraminiferal stable isotope datasets at Site U1334 were placed on a magnetostratigraphic age model calculated by fitting a third-order polynomial through 14 magnetostratigraphic age-depth tie-points. Twelve of these chron boundaries fall within the study interval, are given in Table 1, and are shown in Figs. 3 and 4. This magnetostratigraphic age model yields an initial duration of ~21.9 to 24.1 Ma for the study interval (Fig. 4) [*Channell et al*., 2013; *Beddow et al.,* 2016].

2.4 Spectral analysis

We use the statistical software program AnalySeries [*Paillard et al*., 1996] to conduct spectral analyses on the benthic foraminiferal $\delta^{13}C$ and $\delta^{18}O$ and the $CaCO_3$ datasets in the depth domain, on the magnetostratigraphic age model [*Beddow et al*., 2016], and on both astronomically tuned age model options presented here. Prior to analysis, the $CaCO_3$ content and stable isotope data were re-sampled at 2 and 5 cm in the depth domain, and at 2.5 and 3.0 ky in the age domain, respectively, and trends longer than 6 m, or 600 ky, were removed using a notch-filter [*Paillard et al*., 1996]. Blackman Tukey spectral analysis was used to identify dominant periodicities present within the data, which subsequently were filtered using Gaussian filters. We applied cross-spectral analysis to identify coherency and phase relationships between the eccentricity and the $CaCO_3$, $\delta^{18}O$ and $\delta^{13}C$ chronologies. These calculations were performed at 95% significance. Evolutive spectral analyses, using a sliding Fast Fourier Transform (FFT), were computed using MATLAB.

2.5. Reversal ages based on plate-pair spreading rates

We use previously published magnetic anomaly profiles of tectonic plate pair spreading rates [*Wilson*, 1993] to independently test the astronomical age models for Site U1334. This age comparison method is similar to that previously used to support astronomically tuned age models for the Miocene, Pliocene and Pleistocene [*Hilgen et al*., 1991; *Krijgsman et al*., 1999; *Hüsing et al*., 2007]. We have selected plate pairs with high quality anomaly profiles and relatively high spreading rates. These plate-pairs are in order of decreasing spreading rate: Pacific-Nazca, Pacific-Juan de Fuca, Australia-Antarctic, and Pacific-Antarctic. Data for the Pacific-Nazca pair is limited to the northern part of the system, which is well surveyed from studies of the separation of the Cocos plate from the northern Nazca plate during chron C6Bn [*Lonsdale*, 2005; *Barckhausen et al.,* 2008]. Pacific-Juan de Fuca data are from immediately north of the Mendocino fracture zone. Reversal ages based on these spreading rates are also used in previous timescale calibrations [e.g. *Cande and Kent*, 1992] despite the fact that for the Oligocene-Miocene time interval only the Pacific-plate record has survived and the Juan de Fuca plate was subducted. *Wilson* [1988] interpreted a sudden change of spreading-rate gradient for this pair from south faster prior to C6Cn.2n(o) to north faster after that reversal. The dataset for the Australia-Antarctic pair is similar to that presented by *Cande and Stock* [2004]. It is expanded from that used by *Lourens et al.* [2004] who assigned reversal ages spanning from 18.524 Ma to 23.030 Ma for the chron interval from C5Er (top) to C6Cn.2n (base), based on a linear interpolation of spreading rates of 69.9 mm/yr for this plate pair. Data for Pacific-Antarctic come primarily from more recent surveys near the Menard and Vacquier fracture zones [*Croon et al*., 2008].

3. Results

3.1. Lithologic and paleoclimatic records

The synthetic wt% calcium carbonate record ($CaCO_3$ content wt%) ranges between ~45% and 95%, consistent with the coulometric $CaCO_3$ wt% measurements on discrete samples (Figs. 2, 3). Variability is generally twice as large in the lower Miocene section of the record, between 88.95 and ~102 m CCSF-A (core composite depth below sea floor), varying by ~40% with several minima in the record dipping below 70% (Fig. 3). There is little variability in $CaCO_3$ content, across the OMT, between ~102 and ~106 m CCSF-A. The benthic foraminiferal $\delta^{18}O$ record captures a large, partially transient, shift towards more positive values at the Oligocene-Miocene boundary, with maximum values of ~2.4 ‰ occurring at 104.5 CCSF-A (Fig. 2). After the boundary, both $\delta^{18}O$ and $\delta^{13}C$ values show higher amplitude variability, and more permanent shifts towards higher values [*Beddow et al*., 2016].

3.2. Spectral Analysis in the depth domain

The power spectra of the $CaCO_3$ content record in the depth domain reveal strong spectral peaks at frequencies of 0.20 cycles/m and 0.65 cycles/m (Fig. 3). These frequencies broadly correspond to those found in the benthic foraminferal $\delta^{18}O$ and $\delta^{13}C$ depth series at 0.15 cycles/m and 0.65 cycles/m [*Beddow et al.*, 2016]. High-amplitude cycles with frequencies in the range between ~0.20 and 0.80 cycles/m are present in all datasets with an approximate 1:4 ratio, suggesting a strong influence of eccentricity on the records (i.e. ~110:405 ky cycles). This interpretation of strong eccentricity is supported by the application of the initial magnetostratigraphic age model [*Beddow et al.*, 2016].

4. Astronomical tunings of Site U1334

4.1 Initial age model

As a starting point for astronomical tuning we use an initial magnetostratigraphic age model [*Beddow et al*, 2016; *Channel et al.*, 2013], which is based on the chron reversal ages of the 2012 Geologic Time Scale (GTS2012, [*Vandenberghe et al.*, 2012; *Hilgen et al.*, 2012], see Table 1, Fig. 4.). On this initial age model, (time-evolutive) power spectra demonstrate that the $CaCO_3$ content and benthic foraminiferal $\delta^{18}O$ and $\delta^{13}C$ records are dominated by ~110 ky and 405 ky eccentricity paced cycles, with short intervals of strong responses at higher frequencies (Fig. 5). To further assess the influence of eccentricity on the records from Site U1334, we filter the ~110-ky and 405-ky cycles of the $CaCO_3$ content and $\delta^{13}C$ records (Figs. 6a and 7a). In total, we observe just over five 405-ky cycles in both the filtered $CaCO_3$ content and $\delta^{13}C$ records. There is a notable difference in the number of filtered ~110-ky cycles present between these two datasets. We observe twenty-three ~110-ky cycles in the $CaCO_3$ content record, and twenty-one in the $\delta^{13}C$ record. Visual assessment of the number of cycles is not always straightforward, because not every ~110-ky cycle is expressed equally strong in all data records. In the eccentricity solution for the interval approximately between 21.9 and 24.1 Ma, we count five and a half 405-ky cycles and twenty-two ~110-ky cycles. These numbers are largely in agreement with those obtained from visual assessment and Gaussian filtering.

4.2 Astronomical target curve

For our astronomical target curve, we select Earth's orbital eccentricity. Timeseries analyses on the $CaCO_3$ content, and the benthic foraminiferal $\delta^{18}O$ and $\delta^{13}C$ records in the depth domain, and on the initial age model, indicate that eccentricity is the dominant cycle and that higher-frequency cycles are intermittently expressed (Fig. 5). Additional reasons to select eccentricity as the sole tuning target for the OMT of Site U1334 are the uncertain phase relationships of the data records to precession, and the unknown evolution of tidal dissipation and dynamical ellipticity before 10 Ma [*Zeeden et al*., 2014]. These parameters affect the long-term stability of both the precession and obliquity solutions [*Lourens et al.,* 2004*; Husing et al.,* 2007]. We use the most recent nominal eccentricity solution (i.e., La2011_ecc3L) [*Laskar et al.,* 2011a, 2001b; *Westerhold et al*., 2012b] as tuning target, and for the OMT interval this solution is not significantly different from the La2004 eccentricity solution [*Laskar et al.*, 2004], which was used to generate previous astronomically tuned high-resolution age models for this time interval [*Pälike et al.*, 2006a,b].

4.3. Astronomical age calibration of the OMT from Site U1334

To test different ages and durations of the data from Site U1334, and the leads and lags of climate cycles with respect to eccentricity, we first consider the $CaCO_3$ content record and then the benthic foraminiferal $\delta^{13}C$ record as tuning signals. Both tuning options are underpinned by assumptions of a consistent and linear in-phase relationship between the tuning signal and the eccentricity target. Previously tuned climate records for the OMT have shown that these two datasets represent end-members with respect to phase assumptions, with $CaCO_3$ content showing no lag or the smallest lag with respect to orbital eccentricity, and $\delta^{18}O$ and $\delta^{13}C$ showing increasingly larger lags to the ~110-ky and 405-ky eccentricity cycles [*Liebrand et al.*, 2016, *Pälike et al.*, 2006a, *Pälike et al.*, 2006b]. Thus, by selecting the $CaCO_3$ content record and the benthic foraminiferal $\delta^{13}C$ chronology, we span the full range of tuned ages that different phase-assumptions between eccentricity and proxy data possibly could imply. We expect that the $CaCO_3$ tuned age model is in best agreement with independent ages based on spreading rates, and hence, that benthic foraminiferal $\delta^{13}C$ will show the largest lag with respect to eccentricity.

4.3.1. Astronomical tuning using the $CaCO_3$ content record

We use the initial magnetostratigraphic age model as a starting point for a more detailed ~110-ky calibration of $CaCO_3$ content of the sediment to eccentricity. $CaCO_3$ maxima, mainly reflecting increased surface ocean productivity and/or decreased deep-ocean dissolution [e.g. *Hodell et al.*, 2001], generally correspond to more positive $\delta^{18}O$ values, which are indicative of cooler, glacial periods. Hence, both bulk $CaCO_3$ content and benthic foraminiferal $\delta^{18}O$ values are linked to eccentricity minima and are therefore anticorrelated with eccentricity [*Zachos et al.*, 2001; *Pälike et al.*, 2006a; *Pälike et al.*, 2006b]. The $CaCO_3$ content record is characterized by strong maxima, which we manually aligned to ~110-ky eccentricity minima by visually selecting tie-points (Fig. 6c). In addition to these well expressed ~110-ky cycles, we take the expression of the 405-ky cycle into account to establish the tuned age model. The data records from Site U1334 span the interval between 21.96 and 24.15 Ma (2.19 My duration) on the $CaCO_3$ tuned age model. Linear sedimentation rates (LRS) vary between 0.9 and 2.2 cm/ky (Fig. 6). On average this yields a sample resolution of 3.6 ky for the benthic foraminiferal isotope records.

Evolutive analyses (i.e., FFT using a sliding window) of the $CaCO_3$ content and benthic foraminiferal $\delta^{18}O$ and $\delta^{13}C$ records on the $CaCO_3$ tuned age model indicate that the 405-ky cycle is relatively strongly expressed in all datasets (Fig. 5). However, this signal is weaker or absent across the OMT (~23 Ma) in the evolutive spectrum of $CaCO_3$ content, and post-OMT in benthic foraminiferal $\delta^{18}O$. The ~110-ky cycle is present in the data records on the $CaCO_3$ tuned age model between 23.4 and 22.2 Ma for $CaCO_3$ content, between 23.0 and 22.2 for benthic foraminiferal $\delta^{18}O$, and between 22.8 and 22.2 in benthic foraminiferal $\delta^{13}C$. The ~110-ky cycle is particularly pronounced in in both the $CaCO_3$ and the benthic foraminiferal $\delta^{18}O$ records, and we can identify power at both the 125 ky and the 95 ky eccentricity cycles. We note that this could be a direct result from using eccentricity as a tuning target (see e.g., [*Shackleton et al.,* 1995; *Huybers and Aharonson*, 2010). For $\delta^{13}C$, the evolutive analysis and power spectra indicate that ~110 ky cycle is more strongly expressed at the 125-ky periodicity, compared to the 95-ky component. We find intermittent power present at a periodicity of ~50 ky/cycle, which is either related to the obliquity cycle that is offset towards a slightly longer periodicity, or to the first harmonic of the ~110-ky eccentricity cycle [*King*, 1996]. The ~50-ky cycle is best expressed in the benthic foraminiferal $\delta^{18}O$ record on the $CaCO_3$ tuned age model, where we identify two main intervals with significant power at this periodicity, one between ~23.5 and ~23.8 Ma, and the other between ~22.4 and ~22.6 Ma (Fig. 5).

Cross-spectral analyses between the $CaCO_3$ content, $\delta^{18}O$ and $\delta^{13}C$ records on the $CaCO_3$ tuned age model and eccentricity, indicate that all are significantly coherent at the 405-ky, 125-ky and 95-ky eccentricity cycles (Fig. 5). Phase estimates of benthic foraminiferal $\delta^{18}O$ with respect to eccentricity indicates a lag of 21±16 ky at the 405 ky period, and 9±3 ky at the ~110 ky periodicity (95% confidence on error bars). The $\delta^{13}C$ record lags eccentricity by 29±14 ky at the 405-ky cycle, by 9±4 ky at the ~110-ky cycle (Fig. 5). The coherence between $CaCO_3$ content and eccentricity is only just significant, and phase estimates roughly in-phase with eccentricity; 6±24 ky at the 405 ky cycle, and −1±2 ky at the ~110-ky cycle. These phase estimates between $CaCO_3$ content and eccentricity are not surprising, because $CaCO_3$ content was used to obtain astronomically tuned ages. These phase relationships between $CaCO_3$ and eccentricity thus confirm that the in-phase tuning assumption was applied successfully.

4.3.2. Astronomical tuning using the benthic foraminiferal $\delta^{13}C$ record

An important consequence of the $CaCO_3$ tuned age model is that eccentricity-related variability within the benthic foraminiferal $\delta^{13}C$ record is not in-phase with eccentricity (Fig. 7b; [*Laurin et al.*, 2017]). On both the initial magnetostratigraphic age model and on the $CaCO_3$ tuned age model, the phase-lag, as visually identified in the filtered records, between the 405-ky-eccentricity cycle and the 405-ky cycle in $\delta^{13}C$ increases during the early Miocene (Figs. 6 and 7). The 405-ky eccentricity pacing of $\delta^{13}C$ is a consistent feature that characterizes the Cenozoic carbon cycle [*Holbourn et al*., 2004, 2013; *Littler et al*., 2014; *Pälike et al*., 2006a,b; *Liebrand et al*., 2016], and to date no large changes in phase-relationship have been documented. However, the increased phase lag in the response of the 405-ky cycle in $\delta^{13}C$ to eccentricity, as is suggested by the $CaCO_3$ tuned age model, could provide further support for a large-scale reorganization of the carbon cycle across the OMT as has previously been suggested based on a sudden increase in accumulation rates of benthic foraminifera and Uranium/Calcium values, suggesting increased organic carbon burial [*Diester-Haas et al*., 2011, *Mawbey and Lear*, 2013].

To test the validity of the large phase-lag of the 405-ky cycle in benthic foraminiferal $\delta^{13}C$ to eccentricity, and to test the potential increase of this lag, we generate another astronomically tuned age model. This time, we use the benthic foraminiferal $\delta^{13}C$ record as the tuning signal and assume that the 405-ky cycles and ~110-ky cycles in benthic foraminiferal $\delta^{13}C$ are in-phase with eccentricity across the OMT (Fig. 7d). Approximately five 405-ky cycles are identified in the benthic foraminiferal $\delta^{13}C$ record, which facilitate initial visual alignment to the same cycle in the eccentricity solution. Subsequently, we correlated the maxima and minima in the of the benthic foraminiferal $\delta^{13}C$ record, as identified in Gaussian filters centered around the ~110-ky cycle of this record on the initial magnetostratigraphic age model (Fig. 7a), to those identified in the filtered component of the eccentricity solution (Fig. 7d).

The data records, on the benthic foraminiferal $\delta^{13}C$ tuned age model, span the interval between 22.1 and 24.2 Ma (i.e., 2.1 My duration), resulting in an average time step of 3.4 ky for the benthic stable isotope records. LRS generally range between 0.7 and 2.5

cm/ky, apart from an abrupt and short-lived increase across the OMT to ~3.3 cm/ky. On the $\delta^{13}C$ tuned age model, the $CaCO_3$ record remains in anti-phase with respect to ~110-ky eccentricity, but the benthic foraminiferal $\delta^{13}C$ tuning results in an alternative alignment $CaCO_3$ cycles to eccentricity, yields a ~110-ky shorter duration of the data records, and causes the sudden increase in sedimentation rates across the OMT (Fig. 6 and 7). The evolutive analyses and power spectra are broadly consistent with the evolutive analyses from the $CaCO_3$ tuned age model, with dominant 405-ky cyclicity in all three datasets, an increase in spectral power at ~110-ky eccentricity cycles after the OMT and intermittent expression of higher frequency astronomical cycles (Fig. 5). On the $\delta^{13}C$ tuned age model, all datasets exhibit a relatively stronger response at the 95-ky short eccentricity cycle than the 125-ky short eccentricity cycle, in contrast to the $CaCO_3$ tuned age model. In the late Oligocene, between ~ 23.3 and 23.8 Ma, strong 40-ky obliquity cycles are present in the benthic foraminiferal $\delta^{18}O$ record on the $\delta^{13}C$ tuned age model.

Cross-spectral analyses between the $CaCO_3$ content, $\delta^{18}O$ and $\delta^{13}C$ records on the $\delta^{13}C$ tuned age model and eccentricity, indicate that all are significantly coherent at the 405-, 125- and 95-ky eccentricity cycles (Fig. 5). $CaCO_3$ content leads eccentricity by −24±18 ky at the 405-ky cycle, by −7±3 ky at the ~110-ky cycle. On the $\delta^{13}C$ tuned age model, phase estimates of $\delta^{18}O$ with respect to eccentricity shows small leads of −4±12 ky at the 405-ky cycle, and of −1±4 ky at the ~110-ky cycle. Benthic foraminiferal $\delta^{13}C$ lags eccentricity by 19±8 ky at the 405-ky cycle and by 3±2 ky at the ~110-ky eccentricity cycle, which is congruent with the in-phase tuning assumption between benthic foraminiferal $\delta^{13}C$ and eccentricity that is used in this age model.

4.3.3. Age model comparison

The final eccentricity tuned age models for the OMT time interval differ for two reasons. Firstly, there are 21 complete 110 ky cycles in the $\delta^{13}C$ tuned age model, and 22 in the $CaCO_3$ content record. The tuned age models are largely consistent with each during the late Oligocene and OMT interval. The base of Chron C6Cn.2n, which marks the Oligocene-Miocene boundary, occurs within 10 ky on both age models. The two astronomically tuned age models diverge at ~22.7 Ma, where the $CaCO_3$ content has an additional ~110 ky cycle on the initial magnetostratigraphic age model. A second factor contributing to the difference between the two astronomically tuned age models is the different phase relationships between the two proxy records and eccentricity (i.e., either $CaCO_3$ is in-phase eccentricity, or benthic foraminiferal $\delta^{13}C$). These different phase assumption that underpin the two tuned age models account for age differences up to 10% at all periodicities in the two records (Table 2), in addition to the ~110-ky difference for the early Miocene interval of Site U1334 that results from the two different cyclostratigraphic interpretations. In turn, these interpretations are resultant from the initial phase-assumptions. The longer lag time of $\delta^{13}C$ with respect to eccentricity, in comparison with $CaCO_3$, leads to older ages assigned to ~110 kyr cycles in the $\delta^{13}C$ age model. This is particularly notable between 22.7 Ma and 24.2 Ma, when the difference between the age models is accounted for only by the difference in phase.

5. Spreading rates

To independently test whether the $CaCO_3$ tuned ages or the benthic foraminiferal $\delta^{13}C$ tuned ages and their underlying phase-assumption, are most appropriate for tuning the deep marine Oligocene-Miocene records from Site U1334, we assign the tuned magnetostratigraphic reversal ages from Site U1334 to those identified in anomaly profile of tectonic plate pairs. We use the evolution through time of the spreading rates of these plate pairs as a control for our tuned age models [*Wilson*, 1993; *Krijgsman et al*., 1999]. Rapid simultaneous fluctuations in the spreading rate of multiple plate pairs are highly unlikely and indicate errors in the tuned timescale. We propose to use the astronomically tuned age model from Site U1334 that passes this test most successfully to provide ages for C6Bn.1n (o) to C7n.1r (o) and potentially revise those currently presented in the GTS2012.

On the $CaCO_3$ tuned age model, the Australia-Antarctica, Pacific-Nazca, and Pacific-Antarctic plate pairs are all very close to a constant spreading rate (Fig. 8). The Juan de Fuca-Pacific plate-pair indicates a sudden decrease in spreading rate (145 to 105 mm/yr) at ~23 Ma, consistent with expectations (see the above section **2.5**; [*Wilson*, 1988]). In contrast, the synchronous changes for the Australia-Antarctica, Pacific-Nazca, and Pacific-Antarctic plate pairs in the $\delta^{13}C$ tuned age model, especially the faster spreading rates ~22.5-23.0 Ma implied by older ages for C6Bn, make this tuning option less plausible. Differences between the $CaCO_3$ tuned age model for Site U1334 and GTS2012 are subtler. The longer duration of C6Cn.3n in the $CaCO_3$ tuned age model (106 vs. 62 kyr, Table 1) eliminates a brief, and relatively small, pulse of fast spreading implied by GTS2012, visible in Figure 8a as positive slopes in age-distance during that chron. Over longer intervals, $CaCO_3$ tuned ages remove a slight but synchronous rate slowdown that is also implied by GTS2012 and which starts at ~23.2 Ma.

The $CaCO_3$ tuned age model indicates a duration for C6Cn.2n of 67 ky. This duration may be up to ~40 ky too short, as is suggested by the relatively short-lasting increase in spreading rates during this chron (see the positive slopes in Figure 8b). The spreading-distance error bars indicate that this age discrepancy is marginally significant, with no overlap in reduced distance for the boundaries of this chron for three of four plate pairs. Despite this small uncertainty in the duration for chron C6Cn.2n on the $CaCO_3$ tuned age model, the base of this chron appears in good agreement with spreading rates and thus suggests a slightly older age for the Oligocene-Miocene boundary of approximately 23.06 Ma. Furthermore, the polarity chron ages from the $CaCO_3$ tuned ages are generally older by approximately 40 ky on average than those presented in the GTS2012 (Table 1). In both the $CaCO_3$ content and $\delta^{13}C$ record, the short interval around C6Cn.2n is difficult to align to the eccentricity solution (Figs. 5 and 6), because $CaCO_3$ content values are high, with little variability and benthic foraminiferal $\delta^{13}C$ values corresponds to the marked shift towards higher values at the Oligocene-Miocene carbon maximum [*Hodell and Woodruff*, 1994]. The 83 kyr duration of C6Cn.2n from the $\delta^{13}C$ tuned age model is better supported by spreading rates than the 67 kyr duration from the $CaCO_3$ tuned age model, and the 118 kyr duration in GTS2012 is even more consistent with constant spreading rates. If we extrapolate constant spreading rates across C6Cn.2n, using the $CaCO_3$ tuned age for the base of 23.06 Ma, we obtain an age for the top of this normal polarity interval of ~22.95 Ma, and a duration of 110 ky. An important implication of the $CaCO_3$ tuned ages is the delayed increase in spreading rates of the Juan de Fuca-Pacific plate-pair. On the $CaCO_3$ tuned age model this occurred approximately 200 ky later than those ages presented in the GTS2012 (i.e. during Chron C6Cn.2n. instead of C6Cn.3n, respectively; see Fig 8).

6. Discussion

6.1. Evaluation of tuning signals

Of the two astronomically tuned age models and GTS2012, the $CaCO_3$ tuned age model is most consistent with the assumption of the least amount of changes in plate-pair spreading rates, which makes it the preferred astronomically tuned age model option for Site U1334. (Fig. 8). This agreement between plate pair spreading rate history and the $CaCO_3$ tuned ages, suggests that local/regional (i.e., lithological) tuning signals can produce more accurate age models in comparison with age models based on globally integrated isotope records. The latter data are known to produce significant lags relative to eccentricity as a result of highly nonlinear feedback mechanisms [*Laurin et al*., 2017; *Pälike et al*., 2006b; *Zeebe et al*., 2017]; a result that is confirmed by this study (Table 2). The independent evidence that we provide for using a lithological (proxy) record for astronomical age calibration of marine sediments yields further support for similar astronomical tuning methods. Examples are: the Middle Miocene [*Kochhann et al*., 2016] and Eocene-Oligocene [*Westerhold et al*., 2015] records from the equatorial Pacific Ocean, and the Oligocene-Miocene records from the South Atlantic Ocean [*Liebrand et al*., 2016]. We note, however, that these records show variable ratios of productivity to dissolution as the main source of variance in the data. Future, additional testing of phase-uncertainties could include statistical approaches, such as Monte Carlo simulations [*Khider et al.*, 2017].

6.2 Implications for the carbon cycle

Benthic foraminiferal $\delta^{13}C$ variations in the open ocean are typically interpreted to reflect the ratio between global organic and inorganic carbon burial [*Shackleton*, 1977; *Broecker*, 1982; *Diester-Haas et al*., 2013, *Mawbey and Lear*, 2013]. Astronomical forcing of organic carbon burial is typically expected in the precessional band because organic carbon burial, notably in the marine realm, depends on clay fluxes and thus hydrology [*Berner et al*., 1983]. However, the residence time of carbon (~100 kyr) is so long [*Broecker and Peng*, 1982] that this energy is transferred into eccentricity bands [*Pälike et al*., 2006; *Ma et al*., 2011; *Laurin et al*., 2017]. Importantly, while the total marine carbon inventory is driven by ocean chemistry, the phase lag between eccentricity forcing and $\delta^{13}C$ should primarily be a function of the residence time of carbon [*Zeebe et al.*, 2017]. Hypothetically, a change in total organic matter burial will only result in whole-ocean steady state when the $\delta^{13}C$ of buried carbon equals that of the input (through rivers). Because the burial fluxes are small compared to the total carbon inventory, a pronounced time lag between eccentricity forcing and $\delta^{13}C$ is expected [e.g., *Zeebe et al.*, 2017].

Interestingly, the $CaCO_3$ age model for Site U1334 suggests that the phase lag between the 405 ky cycle in the $\delta^{13}C$ record and the eccentricity forcing increases across the OMT (see position of minima and maxima of the 405 ky filters of eccentricity and benthic foraminiferal $\delta^{13}C$ in Fig. 7). In theory [*Zeebe et al.*, 2017], an increase in the phase lag suggests an increase in the residence time oceanic carbon, either through a rise in the total carbon inventory or a drop in the supply and burial of carbon. The lengthening of the phase lag of the 405 ky cycle coincides with a large shift in the benthic foraminiferal $\delta^{13}C$ record across the OMT to more positive values, evidencing a structural relative increase in the supply of ^{13}C-depleted or drop in the burial of ^{13}C-enriched carbon. Reliable reconstructions of CO_2 are rare across the OMT (www.p-co2.org) and the OMT does not seem associated with a large change in the depth of the Pacific calcite compensation depth [*Pälike et al*., 2012]. Therefore, additional constraints on atmospheric CO_2 concentrations and burial fluxes are required to better understand the climatic/oceanographic mechanisms associated with the increased phase lag.

7. Conclusions

We explore the application of $CaCO_3$ content (estimated from magnetic susceptibility and shipboard coulometry) and benthic foraminiferal $\delta^{13}C$ records as tuning signals for the OMT record at Site U1334 in the eastern equatorial Pacific. These two tunings highlight the importance of carefully considering the implications of tuning choices and assumptions when creating astronomical age models. Spreading rate histories provide independent support for $CaCO_3$ tuned age model. This suggests that lithological signals respond more directly (though still nonlinearly) to eccentricity than the stable isotope signals, for which we find support for a delayed response to astronomical climate forcing. Tuning to $CaCO_3$ provides a valuable method to better understand the (lagged) response in benthic foraminiferal $\delta^{18}O$ and $\delta^{13}C$, which are widely used and reproducible proxies for the global climate/cryosphere system and (marine) carbon cycle. One important implication of the $CaCO_3$ age model is that 405 ky cycle in benthic $\delta^{13}C$ shows a distinct phase lag with respect to orbital eccentricity. Lastly, the $CaCO_3$ age model for Site U1334 provides astronomically calibrated ages for C6Bn.1n to C7n.1r. The polarity chron ages from the $CaCO_3$ tuned ages are generally older by approximately 40 ky on average than those presented in the GTS2012. We suggest that these updated early Miocene ages are incorporated in the next version of the Geologic Time Scale.

Acknowledgements

This research used samples provided by the Integrated Ocean Drilling Program (IODP), collected by the staff, crew and scientists of IODP Expedition 320/321. We thank Dominika Kasjanuk, Arnold van Dijk, Maxim Krasnoperov and Jan Drenth for laboratory assistance. Linda Hinnov kindly provided her evolutive analysis MATLAB script. This research was supported by PalaeoClimate.Science (D.L.), NWO grant 865.10.001 (L.J.L), ERC grants 617462 (D.L.) and 259627 (A.S.), NERC grant NE/G014817 (B.S.W.), and a Marie Curie Career Integration Grant "ERAS". All data, on the preferred $CaCO_3$ tuned age model, can be downloaded from www.pangaea.de, or by following this link: https://doi.pangaea.de/10.1594/PANGAEA.885365 .

Figure Captions

Figure 1. Locations of ODP and IODP drill sites discussed in this study. Location of IODP Site U1334 with reference to ODP Sites 1264, 1218, 926, 929 and 1090.

Figure 2. Calibration between the shipboard magnetic susceptibility record and shipboard coulometric $CaCO_3$ measurements to estimate $CaCO_3$ content. (a) The magnetic susceptibility/$CaCO_3$ content record [*Pälike et al.*, 2010; *Westerhold et al.*, 2012a]. Green area indicates the 2σ uncertainty estimate of the coulometry measurements [*Pälike et al.*, 2010]. Red circles represent shipboard coulometric $CaCO_3$ values. **(b)** The relationship between coulometric $CaCO_3$ measurements and resampled magnetic susceptibility is calculated using ordinary least squares linear regression, and yields an R^2 value of 0.92.

Table 1. Comparison of magnetostratigraphic reversal ages. Chron boundary ages across the Oligocene Miocene Transition from the published literature and this study. Age differences with the GTS2012 age are presented in the lower part of the table. A: [*Lourens et al*., 2004]; B: [*Hilgen et al.*, 2012; *Vandenberghe et al.*, 2012]; C: [*Billups et al.*, 2004]; D & E: [*Pälike et al.*, 2006b]; F: [*Liebrand et al.*, 2016]; G: [*Channell et al.*, 2013]; H & I: [this study].

Figure 3. Site U1334 datasets, evolutive spectra and power spectra against depth. **(a)** Magnetostratigraphy for Site U1334 [*Channell et al.*, 2013]. **(b)** The $CaCO_3$ content record. **(c)** The benthic foraminiferal $\delta^{18}O$ record. **(d)** The benthic foraminiferal $\delta^{13}C$ record. Dashed line marks the base of magnetochron C6Cn.2n; the boundary between the Oligocene and the Miocene. **(e)** Depth-evolutive FFT analysis and power spectra of the $CaCO_3$ content record, **(f)** the benthic foraminiferal $\delta^{18}O$ record, and **(g)** the benthic foraminiferal $\delta^{13}C$ record. All data is presented on the revised splice of *Westerhold et al.* [2012a].

Figure 4. Depth versus age relationships for the different age models for Site U1334. Magnetochron ages are based on GTS2012 [*Vandenberghe et al.*, 2012; *Hilgen et al.*, 2012], the initial age model (i.e., a third order polynomial through the GTS2012 ages), the $CaCO_3$ content age model and the $\delta^{13}C$ age model. Magnetochrons are plotted as colored circles.

Figure 5. **Implication of age models on time series analysis. (a-c)** Time-evolutive FFT analysis of $CaCO_3$ content on the initial magnetostratigraphic age model (i.e., a

third order polynomial), the $CaCO_3$ content tuned age model, and the $\delta^{13}C$ tuned age model, respectively. **(d-f)** As in (a-c) but for benthic foraminiferal $\delta^{18}O$. **(g-i)** As in (a-c) but for benthic foraminiferal $\delta^{13}C$. For all records, periodicities larger than 600 ky are removed using a notch-filter. For panels b to i: coherence with, and phase relationships to, eccentricity (La2011 solution) are depicted. All proxy data records were multiplied by −1 before computing the phase estimates.

Figure 6. Site U1334 $CaCO_3$ versus age. (a) The $CaCO_3$ dataset and 405-ky and ~110-ky Gaussian filters plotted on **(a)** the magnetostratigraphic age model, **(b)** the $\delta^{13}C$ tuned age model, and **(c)** the $CaCO_3$ tuned age model. **(d)** Earth's orbital eccentricity solution is plotted in grey [*Laskar et al*., 2010, *Laskar et al*., 2011]. Tie points are represented by red dots and dashed lines. Gaussian filters were calculated in AnalySeries [*Palliard et al*., 1996] with the following settings: 405 ky *– f : 2.5 bw 0.8,* ~110 ky *– f : 10, bw : 3.* **(e)** Sedimentation rates are calculated using the $CaCO_3$ tuned age model.

Figure 7. **Site U1334 $\delta^{13}C$ versus age.** The $\delta^{13}C$ dataset and 405-ky and ~110-ky Gaussian filters plotted on **(a)** the magnetostratigraphic age model, **(b)** the $CaCO_3$ tuned age model, and **(c)** the $\delta^{13}C$ tuned age model. **(d)** Earth's orbital eccentricity solution is plotted in grey [*Laskar et al*., 2010, *Laskar et al*., 2011]. Tie points are represented by red dots and dashed lines. Gaussian filters were calculated in AnalySeries [*Palliard et al*., 1996] with the following settings: 405 ky *– f : 2.5 bw 0.8,* ~110 ky *– f : 10, bw : 3.* **(e)** Sedimentation rates are calculated using the $\delta^{13}C$ tuned age model.

Table 2. Comparison of tuning methods and phase relationships. List of astronomically dated Oligocene-Miocene spanning record. Tuning signal (i.e., lithological or climatic proxy records) and target curves (i.e., astronomical solutions), and phase relationships to the target curves are compared. Please note: not all records span the same time interval, and that time-average, mid-phase estimates are given. A: [*Billups et al.*, 2004], B: [*Pälike et al.*, 2006a], C: [*Pälike et al.*, 2006b], D: [*Liebrand et al.*, 2016], for time-evolutive phase-estimates of benthic foraminiferal $\delta^{18}O$ with respect to eccentricity see [*Liebrand et al.*, 2017], E & F: [this study].

Figure 8. **Plate-pair spreading rates based on different age models.** Reduced-distance plots for the labeled plate pairs implied by **(a)** the GTS2012, **(b)** the $CaCO_3$ tuned age model and **(c)** the $\delta^{13}C$ tuned age model. Reduced distance is the full spreading distance (D) minus the age (A) times the labeled spreading rate (R, see y-axes). Distance scale is plotted inversely with spreading rate. This results in age errors that depart vertically from a straight line, when spreading rates are constant. Inset scale bar shows the vertical offset resulting from a 100-kyr change in a reversal age. Dashed horizontal lines are viewing aids to evaluate the prediction that constant spreading at the reduction rate R will produce a horizontal line. Error bars are 95% confidence. The $CaCO_3$ based age model **(b)** gives the simplest spreading rate history and represents the preferred tuning option.

References

Barckhausen, U., C. R. Ranero, S. C. Cande, M. Engels and W. Weinrebe (2008), Birth of an intraoceanic spreading center. *Geology*, *36*(10), 767-770.

Beddow, H. M., D. Liebrand, A. Sluijs, B. S. Wade, and L. J. Lourens (2016), Global change across the Oligocene-Miocene transition: High-resolution stable isotope records from IODP Site U1334 (equatorial Pacific Ocean), *Paleoceanography, 31, doi:10.1002/2015PA002820.*

Berner, R. A., A. C. Lasaga, and R. M. Garrels (1983), The carbonate-silicate geochemical cycle and its effect on atmospheric carbon dioxide over the past 100 million years. *American Journal of Science, 283,* 641–683, doi: 10.2475/ajs.283.7.641.

Billups, K., H. Pälike, J. E. T. Channell, J. C. Zachos, and N. J. Shackleton (2004), Astronomic calibration of the late Oligocene through early Miocene geomagnetic polarity time scale, *Earth Planet. Sci. Lett.*, *224*, 33–44, doi:10.1016/j.epsl.2004.05.004.

Broecker, W. S. (1982), Glacial to interglacial changes in ocean chemistry, *Progress in Oceanography*, 11, 2, 151-197.

Broecker, W. S., T-H Peng (1982), Tracers in the Sea, Lamont-Doherty Geological Observatory, Columbia University.

Cande, S. C., and D. V. Kent (1992), A new geomagnetic polarity time scale for the Late Cretaceous and Cenozoic, *J. Geophys. Res.*, *97*(B10), 13917-13951.

Cande, S. C., and J. M. Stock (2004), Pacific-Antarctic-Australia motion and the formation of the Macquarie plate, *J. Geophys. Int.*, 157, 399-414.

Channell, J .E. T., C. Ohneiser, Y. Yamamoto, and M.S. Kesler (2013), Oligocene-Miocene magnetic stratigraphy carried by biogenic magnetite at sites U1334 and U1335 (equatorial Pacific ocean) *Geochemistry, Geophysics, Geosystems, 14*(2) pp1525-2027doi:10.1029/2012GC004429.

Croon, M. B., S. C. Cande, and J. M. Stock (2008), Revised Pacific-Antarctic plate motions and geophysics of the Menard Fracture Zone: *Geochemistry, Geophysics, Geosystems*, v. 9, Q07001, doi:10.1029/2008GC002019.

DeConto, R.M., S. Galeotti, M. Pagani, D. Tracy, K. Schaefer, T. Zhang, D. Pollard, and J.D. Beerling, (2012). Past extreme warming events linked to massive carbon release from thawing permafrost. *Nature*, *484*(7392), p.87.

Diester-Haass, L., K. Billups, and K. Emeis (2011), Enhanced paleoproductivity across the Oligocene/Miocene boundary as evidenced by benthic foraminiferal accumulation rates. *Palaeogeography, Palaeoclimatology, Palaeoecology* 302, 464 - 473 doi:10.1016/j.palaeo.2011.02.006

Diester-Haass, L., K. Billups, I. Jacquemin, K.C. Emeis, V. Lefebvre and L. François, (2013). Paleoproductivity during the middle Miocene carbon isotope events: A data-model approach. *Paleoceanography*, *28*(2), 334-346.

Gradstein, F. M., J. G. Ogg, M. D. Schmitz and G. M. Ogg (2012), *The geologic time scale 2012*.

Herbert, T. D (1994), Reading orbital signals distorted by sedimentation: models and examples. *Orbital forcing and cyclic sequences*, 483-507.

Hilgen, F. J., L. J. Lourens, and J. A. Van Dam (2012), The Neogene Period. *The geologic time scale*, *2*, 923-978.

Hodell, D. A., and F. Woodruff (1994), Variations in the strontium isotopic ratio of seawater during the Miocene: Stratigraphic and geochemical implications. *Paleoceanography* **9**, 405-426.

Hodell, D.A., C.D. Charles and F.J. Sierro (2001), Late Pleistocene evolution of the ocean's carbonate system. *Earth and Planetary Science Letters*, *192*(2), pp.109-124.

Holbourn, A., W. Kuhnt, J. T. Simo and Q. Li (2004), Middle Miocene isotope stratigraphy and paleoceanographic evolution of the northwest and southwest Australian margins (Wombat Plateau and Great Australian Bight). *Palaeogeography, Palaeoclimatology, Palaeoecology*, *208*(1), 1-22.

Holbourn, A., W. Kuhnt, S. Clemens, W. Prell, and N. Andersen (2013), Middle to late Miocene stepwise climate cooling: Evidence from a high-resolution deepwater isotope curve spanning 8 million years, *Paleoceanography, 28*, doi:10.1002/2013PA002538.

Huybers, P., O. Aharonson, 2010. Orbital tuning, eccentricity, and the frequency modulation of climatic precession. Paleoceanography 25. doi:10.1029/2010PA001952

Hüsing, S. K., F. J. Hilgen, H. Abdul Aziz, and W. Krijgsman (2007), Completing the Neogene geological time scale between 8.5 and 12.5 Ma, *Earth and Planetary Science Letters*, *253*, 340-358.

Khider, D., S. Ahn, L.E. Lisiecki, C.E. Lawrence, M. Kienast, M., 2017. The role of uncertainty in estimating lead/lag relationships in marine sedimentary archives: A case study from the tropical Pacific. Paleoceanography 2016PA003057. doi:10.1002/2016PA003057

King, T. (1996). Quantifying nonlinearity and geometry in time series of climate. *Quaternary Science Reviews*, *15*(4), 247-266.

Krijgsman, W., F. J. Hilgen, I. Raffi, F. J. Sierro and D. S Wilson (1999), Chronology, causes and progression of the Messinian salinity crisis. *Nature*, *400*(6745), 652-655.

Kochhann, K. G., Holbourn, A., Kuhnt, W., Channell, J. E., Lyle, M., Shackford, J. K., Andersen, N. (2016). Eccentricity pacing of eastern equatorial Pacific carbonate dissolution cycles during the Miocene Climatic Optimum. *Paleoceanography*, *31*(9), 1176-1192.

Laskar, J., P. Robutel, F. Joutel, M. Gastineau, A. C. M Correia, and B. Levrard (2004), A long-term numerical solution for the insolation quantities of the Earth. *Astronomy & Astrophysics*, *428*(1), 261-285.

Laskar, J., A. Fienga, M. Gastineau, and H. Manche (2011a), La2010: A new orbital solution for the long term motion of the Earth, *Astronomy and Astrophysics*, *532*(A89).

Laskar, J., M. Gastineau, J.-B. Delisle, A. Farrés, and A. Fienga (2011b), Strong chaos induced by close encounters with Ceres and Vesta, *Astronomy and Astrophysics*, *532*(L4), 1-4.

Laurin, J., B. Růžek, M. Giorgioni, (2017). Orbital signals in carbon isotopes: phase distortion as a signature of the carbon cycle. Paleoceanography 2017PA003143. doi:10.1002/2017PA003143

Liebrand, D., L. Lourens, D. A. Hodell, B de. Boer, R. S. W. van der Wal, and H. Pälike (2011), Antarctic ice sheet and oceanographic response to eccentricity forcing in the early Miocene. *Climates of the past, 7*, pp 869 - 880.

Liebrand, D., H. M. Beddow, L. J. Lourens, H. Pälike, I. Raffi, S. M. Bohaty, F. J. Hilgen, Mischa J. M. Saes., P.A. Wilson, A. E. van Dijk, D. A. Hodell, D.

Kroon., C. E. Huck and S. J. Batenburg (2016). Cyclostratigraphy and eccentricity tuning of the early Oligocene through early Miocene (30.1-17.1 Ma): Cibicides mundulus stable oxygen and carbon isotope records from Walvis Ridge Site 1264. *Earth and Planetary Science Letters, 450*, 392-405.

Liebrand, D., A.T.M. de Bakker, H.M. Beddow, P.A. Wilson, S.M. Bohaty, G. Ruessink, H. Pälike, S.J. Batenburg, F.J. Hilgen, D.A. Hodell, C.E. Huck, D. Kroon, I. Raffi, M.J.M. Saes, A.E. van Dijk, and L.J. Lourens, (2017). Evolution of the early Antarctic ice ages. *Proceedings of the National Academy of Sciences of the United States of America*, *114(15)*, 3867-3872.

Littler, K., U. Röhl, T. Westerhold, and J.C. Zachos (2014). A high-resolution benthic stable-isotope record for the South Atlantic: Implications for orbital-scale changes in Late Paleocene–Early Eocene climate and carbon cycling. *Earth and Planetary Science Letters*, *401*, 18-30.

Lonsdale, P., (2005), Creation of the Cocos and Nazca plates by fission of the Farallon plate: *Tectonophysics*, v. 404, p. 237–264, doi: 10.1016/ j.tecto.2005.05.011.

Lourens, L. J., F. J. Hilgen, N. J. Shackleton, J. Laskar and D. Wilson (2004),'Chapter 21: The Neogene Period'. In: Gradstein, F., Ogg, J. and Smith,A., (eds).,*A Geologic Time Scale 2004*, Cambridge University Press, Cambridge, pp. 409-440.

Ma, W., J. Tian, Q. Li, and P. Wang (2011), Simulation of long eccentricity (400-kyr) cycle in ocean carbon reservoir during Miocene Climate Optimum: Weathering and nutrient response to orbital change, *Geophys. Res. Lett., 38*, L10701, doi:10.1029/2011GL047680.

Paillard, D., L. Labeyrie, and P. Yiou (1996), Macintosh program performs time-series analysis, *Eos Trans. AGU*, *77*, 379, doi:10.1029/96EO00259.

Pälike, H., J. Frazier, and J.C. Zachos (2006a), Extended orbitally forced palaeoclimatic records from the equatorial Atlantic Ceara Rise. *Quaternary Science Reviews,* 25, 3138–3149.

Pälike, H., R. N. Norris, J. Herrle, P. A. Wilson, H. K. Coxall, C. H. Lear, N. J. Shackleton, A. K. Tripati, and B. S. Wade (2006b), The heartbeat of the Oligocene climate system, *Science, 314*, 1894–1898, doi:10.1126/science.1133822.

Pälike, H., M. W. Lyle, H. Nishi, I. Raffi, K. Gamage, A. Klaus and the Expedition 320/321 Scientists (2010), *Proceedings of the Integrated Ocean Drilling Program*, Volume 320/321. Tokyo (Integrated Ocean Drilling Program Management International, Inc.).

Pälike, H., M. W. Lyle, H. Nishi, I. Raffi, A. Ridgewell, K. Gamage, et al (2012), A Cenozoic record of the equatorial Pacific carbonate compensation depth, *Nature*, *488*(7413), 609-614.

Shackleton, N . J. (1977), Carbon-13 in Uvigerina: Tropical rain forest history and the equatorial Pacific carbonate dissolution cycles, in *The Fate of Fossil Fuel CO_2 in the Oceans*, edited by N.R. Andersen and A. Malahoff, 401-427, Plenum, New York,

Shackleton, N.J., T.K. Hagelberg, S.J. Crowhurst, 1995. Evaluating the success of astronomical tuning: Pitfalls of using coherence as a criterion for assessing pre-Pleistocene timescales. Paleoceanography 10, 693–697. doi:10.1029/95PA01454

Shackleton, N. J., S. J. Crowhurst, G. P. Weedon, and J. Laskar (1999), Astronomical Calibration of Oligocene-Miocene Time, *Philosophical Transactions: Mathematical, Physical and Engineering Sciences*, *357*(1757), 1907-1929.

Shackleton, N.J., M. A. Hall, I. Raffi, L. Tauxe, and J. C. Zachos (2000), Astronomical calibration age for the Oligocene/Miocene boundary. *Geology 28* (5), 447–450.

Vandenberghe, N., F. J. Hilgen, and R. P. Speijer (2012), The paleogene period. *The geologic time scale*, *2012*, 855-921.

Westerhold, T., et al. (2012a), Revised composite depth scales and integration of IODP Sites U1331–U1334 and ODP Sites 1218–1220, in *Proceedings of the*

Integrated Ocean Drilling Program, vol. 320/321, edited by H. Pälike et al., Integ. Ocean Drill. Progr. Manage. Int., College Station, Tex.

Westerhold, T., U. Röhl and J. Laskar (2012b), Time scale controversy: Accurate orbital calibration of the early Paleogene. *Geochemistry, Geophysics, Geosystems*, *13*(6).

Westerhold, T., Röhl, U., Frederichs, T., Agnini, C., Raffi, I., Zachos, J. C., and Wilkens, R. H. (2017). Astronomical Calibration of the Ypresian Time Scale: Implications for Seafloor Spreading Rates and the Chaotic Behaviour of the Solar System?, Clim. Past Discuss., doi:10.5194/cp-2017-15.

Wilson, D. S. (1988). Tectonic history of the Juan de Fuca ridge over the last 40 million years. *Journal of Geophysical Research: Solid Earth (1978–2012)*, *93*(B10), 11863-11876.

Wilson, D. S. (1993), Confirmation of the astronomical calibration of the magnetic polarity time scale from rates of sea-floor spreading, *Nature, 364*, 788-790.

Zachos, J. C., N. J. Shackleton, J. S. Revenaugh, H. Pälike, and B. P. Flower (2001), Climate response to orbital forcing across the Oligocene – Miocene boundary, *Science* 292, 274– 278.

Zeebe, R. E., T. Westerhold, K. Littler, J. C. Zachos (2017), Orbital forcing of the Paleocene and Eocene carbon cycle, *Paleoceanography, 32,* 440–465, doi:10.1002/2016PA003054.

Zeeden, C., F. J. Hilgen, S. K. Hüsing, and L. J. Lourens (2014), The Miocene astronomical time scale 9–12 Ma: new constraints on tidal dissipation and their implications for paleoclimatic investigations. *Paleoceanography*, *29*(4), 296-307.

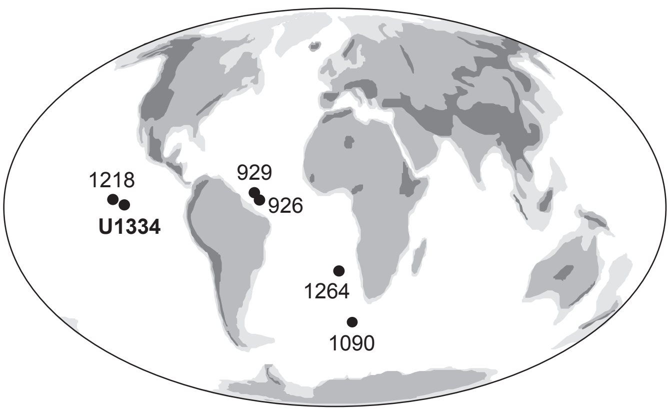
1218
U1334
929
926
1264
1090

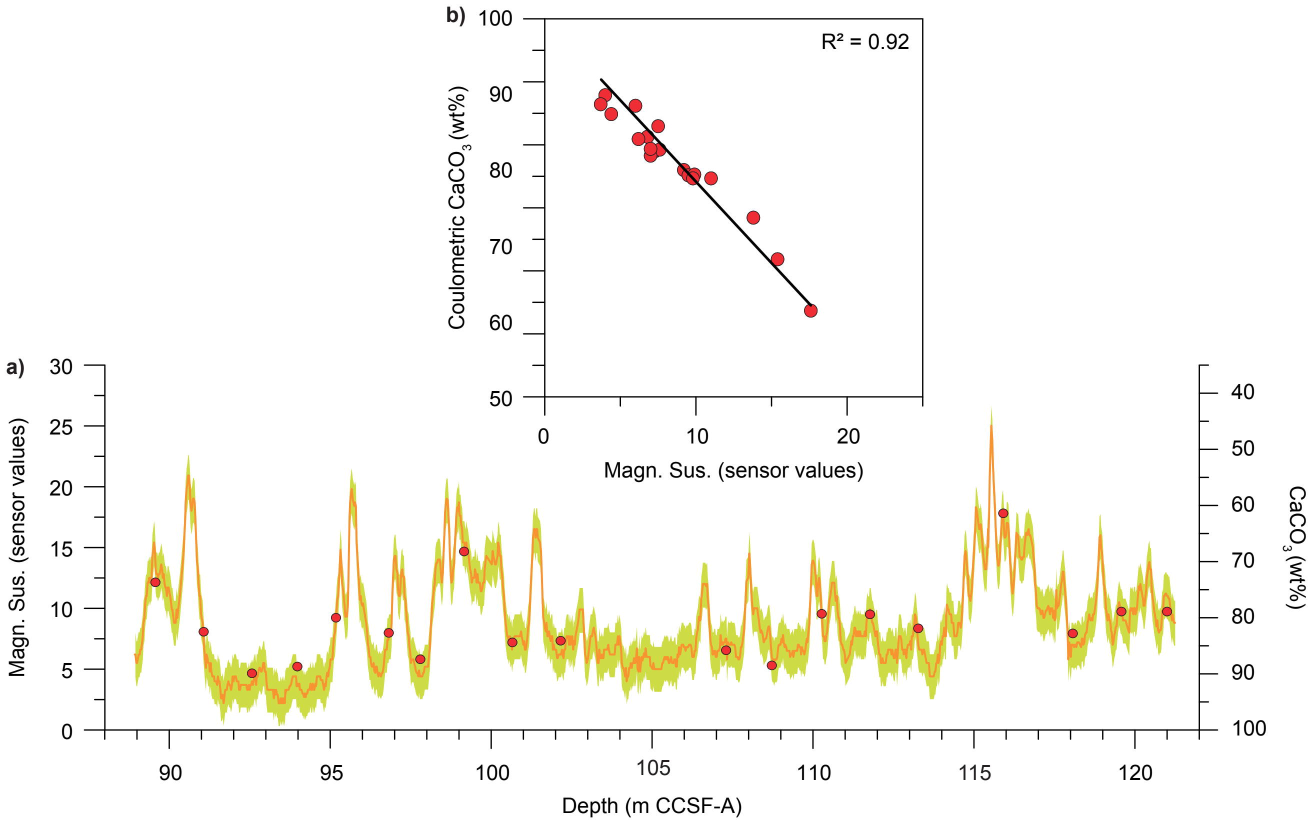

b)
R² = 0.92
Coulometric CaCO3 (wt%)
Magn. Sus. (sensor values)
a)
Magn. Sus. (sensor values)
CaCO3 (wt%)
Depth (m CCSF-A)

Table 1

Chron	A: Age GTS2004 (Ma)	B: Age GTS2012 (Ma)	C: 1090 Tuned age (Ma)	D: 1218 Manual tuned age (Ma)	E: 1218 Auto tuned age (Ma)	F: 1264 Mid tuned age (Ma)	G: U1334 Depth CCSF-A (m)	H: U1334 CaCO3 tuned age (Ma)	I: U1334 δ13C tuned age (Ma)
C6Bn.1n (o)	21.936	21.936	21.991	22.010	21.998		89.17	21.985	22.115
C6Bn.1r (o)	21.992	21.992	22.034	22.056	22.062		89.79	22.042	22.165
C6Bn.2n (o)	22.268	22.268	22.291	22.318	22.299	22.300	94.72	22.342	22.473
C6Br (o)	22.564	22.564	22.593	22.595	22.588	22.608	98.26	22.621	22.697
C6Cn.1n (o)	22.754	22.754	22.772	22.689	22.685	22.760	100.00	22.792	22.809
C6Cn.1r (o)	22.902	22.902	22.931	22.852	22.854	22.944	102.50	22.973	22.970
C6Cn.2n (o)	23.030	23.030	23.033	23.024	23.026	23.052	103.96	23.040	23.053
C6Cn.2r (o)	23.249	23.233	23.237	23.233	23.278	23.247	107.50	23.212	23.211
C6Cn.3n (o)	23.375	23.295	23.299	23.295	23.340	23.332	108.68	23.318	23.286
C6Cr (o)	24.044	23.962	23.988	23.962	24.022		119.10	24.025	24.026
C7n.1n (o)	24.102	24.000	24.013	24.000	24.062		119.58	24.061	24.066
C7n.1r (o)	24.163	24.109	24.138	24.109	24.147		120.76	24.124	24.161

(continued)

Chron	Δ B−C Age (ky)	Δ B−D Age (ky)	Δ B−E Age (ky)	Δ B−F Age (ky)	Δ B−H Age (ky)	Δ B−I Age (ky)
C6Bn.1n (o)	-55	-74	-62		-49	-179
C6Bn.1r (o)	-42	-64	-70		-50	-173
C6Bn.2n (o)	-23	-50	-31	-32	-74	-205
C6Br (o)	-29	-31	-24	-44	-57	-133
C6Cn.1n (o)	-18	65	69	-6	-38	-55
C6Cn.1r (o)	-29	50	48	-42	-71	-68
C6Cn.2n (o)	-3	6	4	-22	-10	-23
C6Cn.2r (o)	-4	0	-45	-14	21	22
C6Cn.3n (o)	-4	0	-45	-37	-23	9
C6Cr (o)	-26	0	-60		-63	-64
C7n.1n (o)	-13	0	-62		-61	-66
C7n.1r (o)	-29	0	-38		-15	-52

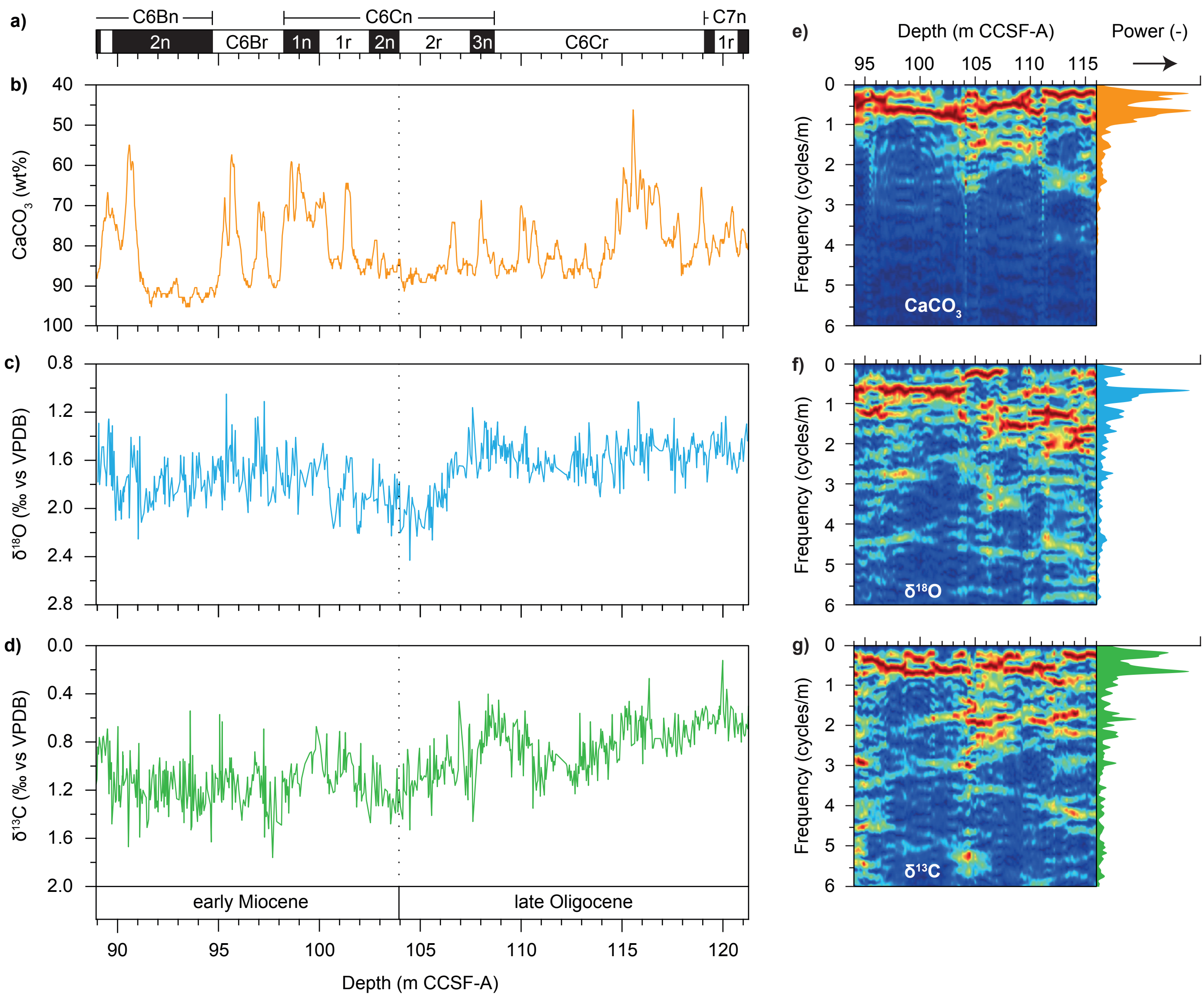

a)
C6Bn
C6Cn
C7n
2n
C6Br
1n
1r
2n
2r
3n
C6Cr
1r
b)
CaCO3 (wt%)
c)
δ18O (‰ vs VPDB)
d)
δ13C (‰ vs VPDB)
early Miocene
late Oligocene
Depth (m CCSF-A)
e)
Depth (m CCSF-A)
Power (-)
Frequency (cycles/m)
CaCO3
f)
δ18O
g)
δ13C

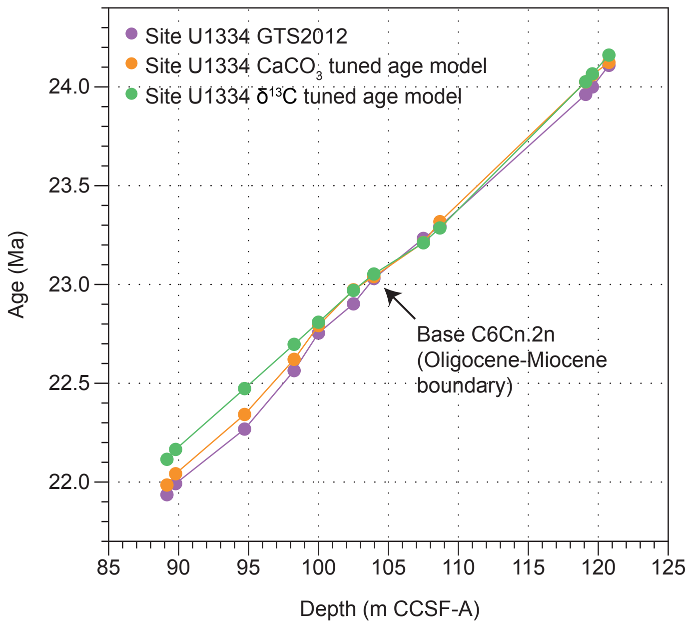

Site U1334 GTS2012
Site U1334 $CaCO_3$ tuned age model
Site U1334 $\delta^{13}C$ tuned age model
Base C6Cn.2n
(Oligocene-Miocene
boundary)
Age (Ma)
24.0
23.5
23.0
22.5
22.0
85
90
95
100
105
110
115
120
125
Depth (m CCSF-A)

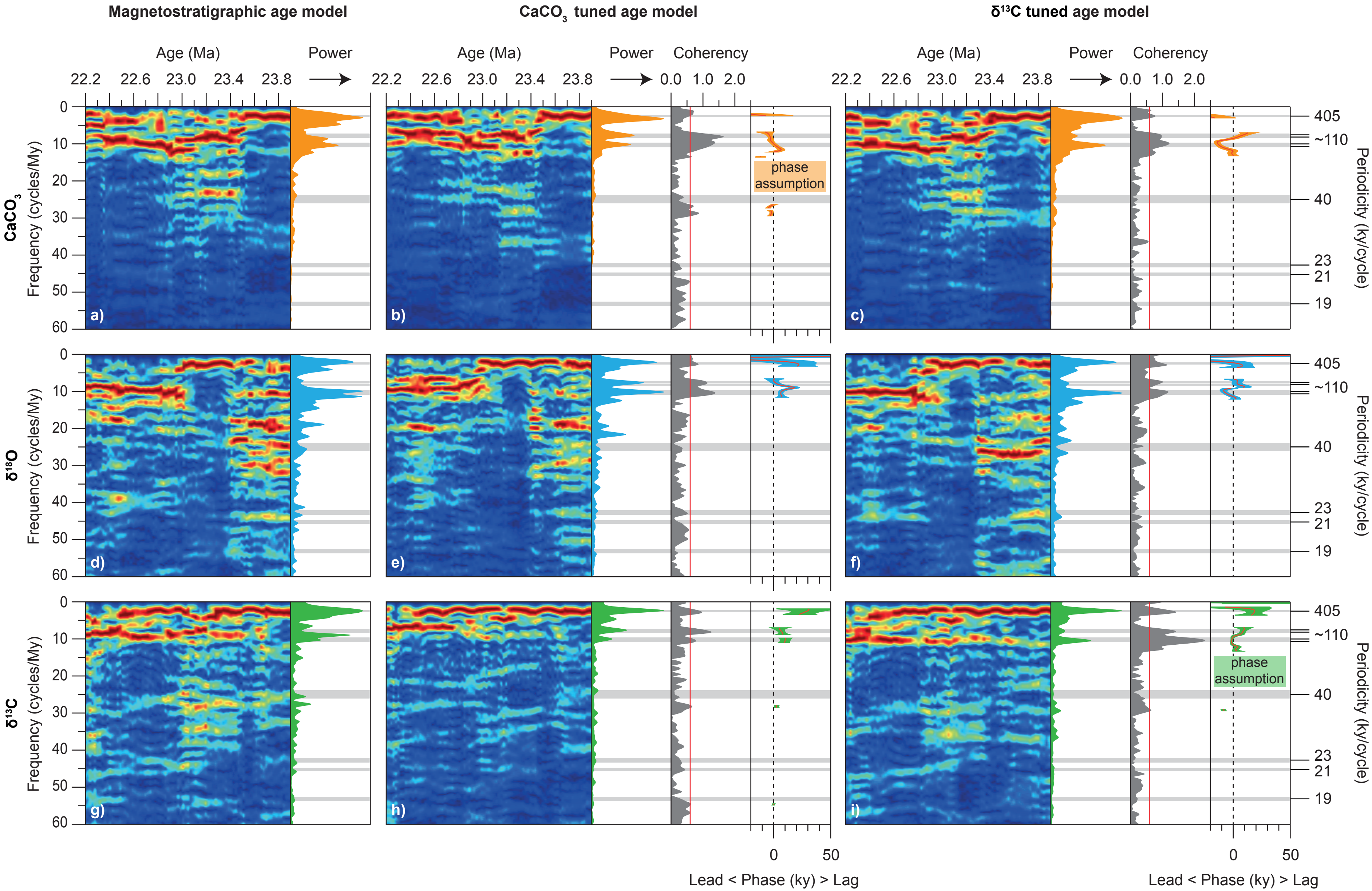

Magnetostratigraphic age model
$CaCO_3$ tuned age model
$\delta^{13}C$ tuned age model
Age (Ma)
Power
Coherency
22.2 22.6 23.0 23.4 23.8
0.0 1.0 2.0
$CaCO_3$
$\delta^{18}O$
$\delta^{13}C$
Frequency (cycles/My)
Periodicity (ky/cycle)
405
~110
40
23
21
19
phase assumption
phase assumption
a)
b)
c)
d)
e)
f)
g)
h)
i)
0 50
Lead < Phase (ky) > Lag

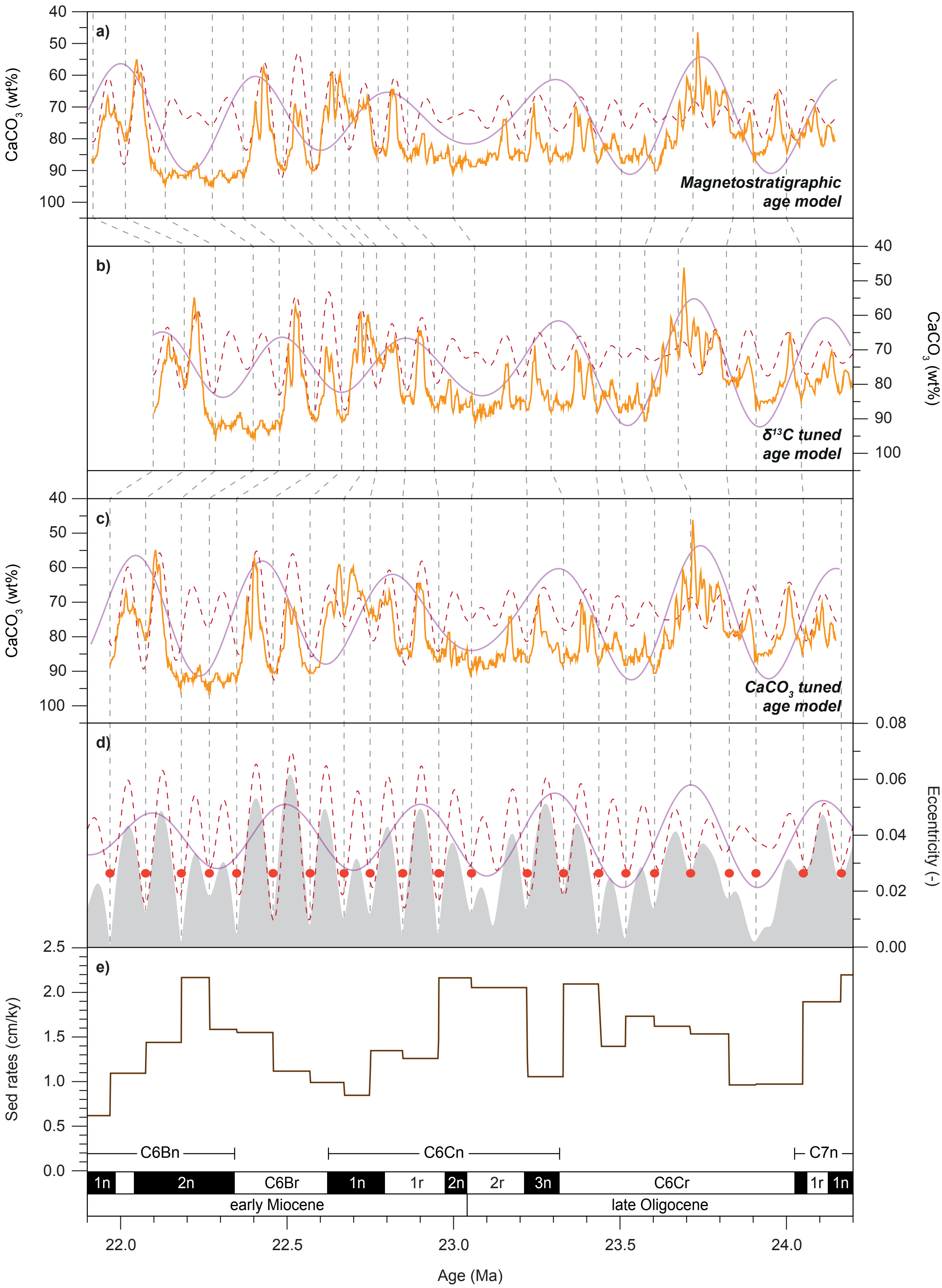

a)
b)
c)
d)
e)
CaCO3 (wt%)
Magnetostratigraphic age model
δ13C tuned age model
CaCO3 tuned age model
Eccentricity (-)
Sed rates (cm/ky)
C6Bn
C6Cn
C7n
1n
2n
C6Br
1n
1r
2n
2r
3n
C6Cr
1r
1n
early Miocene
late Oligocene
22.0
22.5
23.0
23.5
24.0
Age (Ma)

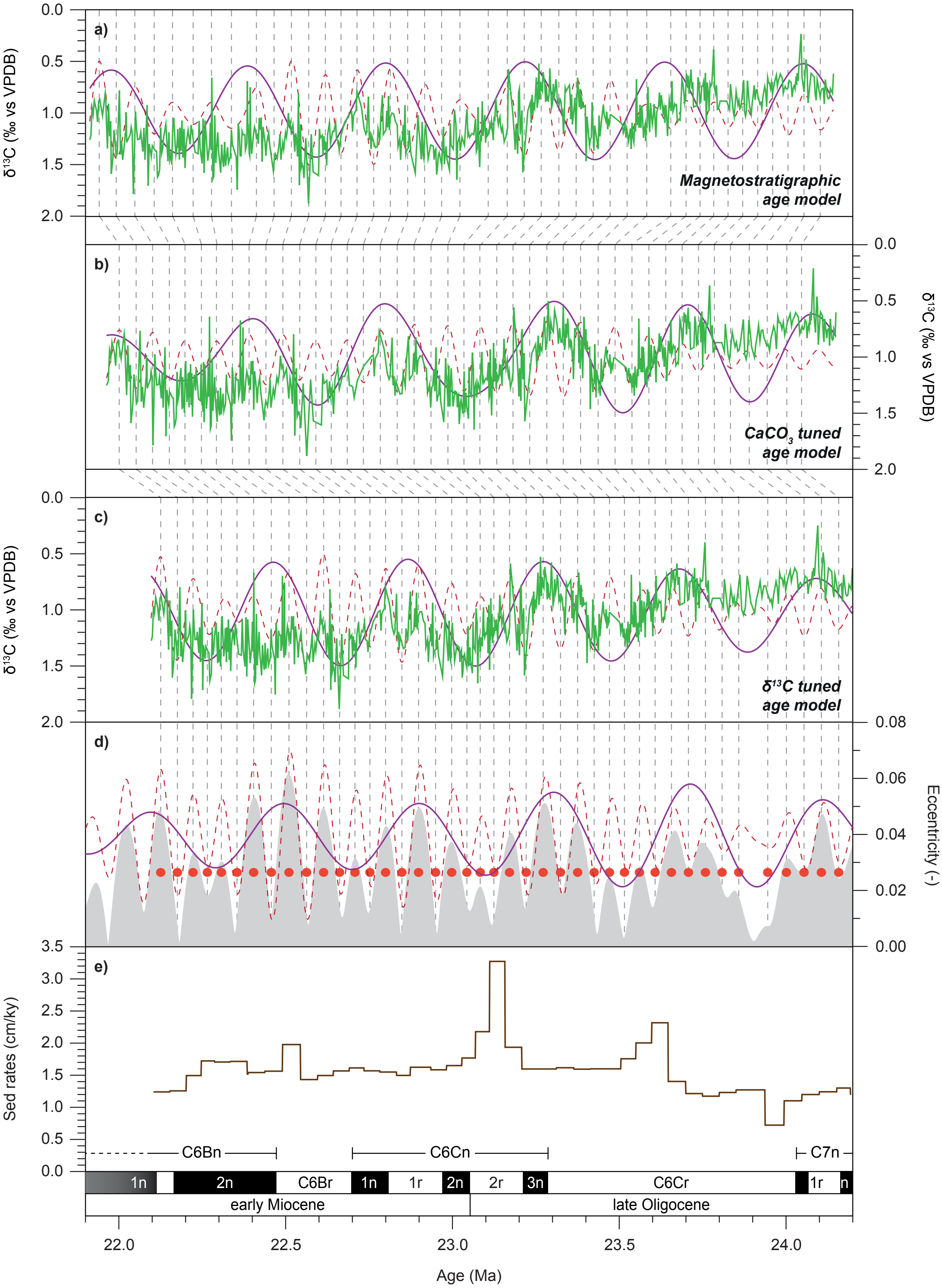

a)
Magnetostratigraphic age model
b)
CaCO3 tuned age model
c)
δ13C tuned age model
d)
e)
δ13C (‰ vs VPDB)
Eccentricity (-)
Sed rates (cm/ky)
C6Bn
C6Cn
C7n
1n
2n
C6Br
1n
1r
2n
2r
3n
C6Cr
1r
n
early Miocene
late Oligocene
22.0
22.5
23.0
23.5
24.0
Age (Ma)

Table 2

Site	Tuning signal	Tuning target	Age range	Lead(−)/ Lag(+) 405 ky $CaCO_3$ content	Lead(−)/ Lag(+) ~110 ky $CaCO_3$ content	Lead(−)/ Lag(+) 405 ky $\delta^{18}O$	Lead(−)/ Lag(+) ~110 ky $\delta^{18}O$	Lead(−)/ Lag(+) 405 ky $\delta^{13}C$	Lead(−)/ Lag(+) ~110 ky $\delta^{13}C$
A: 1090	Benthic foram. $\delta^{18}O$	E/O/P (mainly obliquity)	24–20 Ma	-	-	In phase	+5 ky	+25 ky	+10 ky
B: 926/929	$CaCO_3$ content*	E/O/P (mainly obliquity)	26–17 Ma	-	-	+10 ky	+25 ky	+35 ky	+28 ky
C: 1218	Benthic foram. $\delta^{13}C$	E/O/P (mainly eccentricity)	34–22 Ma	-	-	+8 ky	~In phase	+25 ky	~In phase
D: 1264	$CaCO_3$ content**	Eccentricity	30–17 Ma	Unstable phase	In phase	−14 ky	+12 ky	+36 ky	+12 ky
E: U1334	$CaCO_3$ content***	Eccentricity	24–22 Ma	+6 ky	In phase	+21 ky	+9 ky	+29 ky	+9 ky
F: U1334	Benthic foram. $\delta^{13}C$	Eccentricity	24–22 Ma	−24 ky	−7 ky	−4 ky	In phase	+19 ky	~In phase

*magnetic susceptibility and color reflectance
**natural logarithm of (X-ray fluorescence) Ca over Fe counts
***magnetic susceptibility

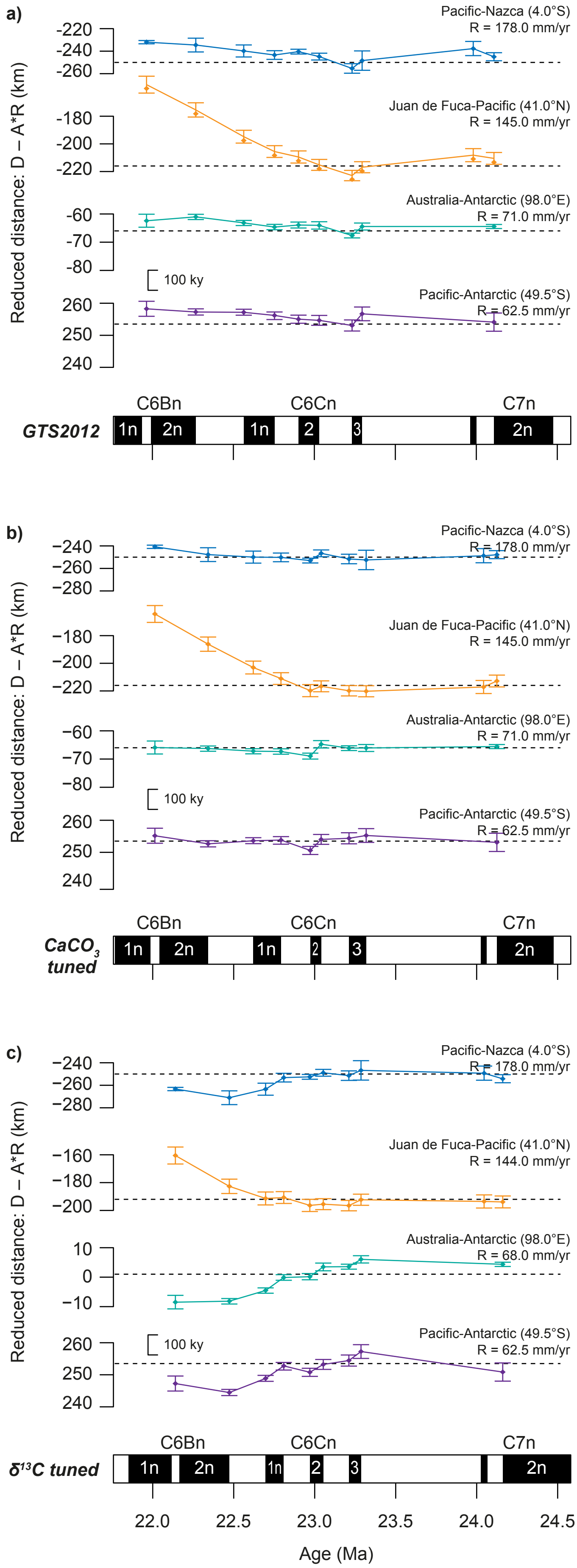

a)
Pacific-Nazca (4.0°S)
R = 178.0 mm/yr
Juan de Fuca-Pacific (41.0°N)
R = 145.0 mm/yr
Australia-Antarctic (98.0°E)
R = 71.0 mm/yr
Pacific-Antarctic (49.5°S)
R = 62.5 mm/yr
100 ky
Reduced distance: D – A*R (km)
C6Bn
C6Cn
C7n
GTS2012
b)
Pacific-Nazca (4.0°S)
R = 178.0 mm/yr
Juan de Fuca-Pacific (41.0°N)
R = 145.0 mm/yr
Australia-Antarctic (98.0°E)
R = 71.0 mm/yr
Pacific-Antarctic (49.5°S)
R = 62.5 mm/yr
CaCO3 tuned
c)
Pacific-Nazca (4.0°S)
R = 178.0 mm/yr
Juan de Fuca-Pacific (41.0°N)
R = 144.0 mm/yr
Australia-Antarctic (98.0°E)
R = 68.0 mm/yr
Pacific-Antarctic (49.5°S)
R = 62.5 mm/yr
δ13C tuned
Age (Ma)